A Ligand Field Model for MCD Spectra of Biological Cupric Complexes

Gregory A. Landrum, Christopher A. Ekberg, and James W. Whittaker
Department of Chemistry, Carnegie Mellon University, Pittsburgh, Pennsylvania 15213 USA

ABSTRACT A ligand field calculation of magnetic circular dichroism (MCD) spectra is described that provides new insights into the information contained in electronic spectra of copper sites in metalloenzymes and synthetic analogs. The ligand field model uses metal-centered p- and f-orbitals to model σ,π LMCT mixing mechanism for intensity, allowing the basic features of optical absorption, MCD, and electron paramagnetic resonance spectra to be simultaneously computed from a single set of parameters and the crystallographically determined ligand coordinates. We have used the model to predict changes in spectra resulting from the transformation of electronic wavefunctions under systematic variation in geometry in pentacoordinate ML_5 complexes. The effectiveness of the calculation is demonstrated for two synthetic copper model compounds and a galactose oxidase enzyme complex representing limiting coordination geometries. This analysis permits immediate recognition of characteristic patterns of MCD intensity and correlation with geometry. A complementarity principle between MCD and CD spectra of transition metal complexes is discussed.

INTRODUCTION

Magnetic circular dichroism (MCD) spectroscopy is a valuable tool for spectroscopic studies of electronic structure of metalloenzyme complexes contributing insight into the electronic origins of catalytic activity. The sensitivity of the method, both for detecting weak spectra and for resolving broad and overlapping absorption features, gives MCD spectroscopy a special advantage in bioinorganic applications, particularly for paramagnetic complexes where results from MCD studies complement electron paramagnetic resonance (EPR) experiments in measuring ground state magnetic properties (Johnson et al., 1982; Sutherland and Holmquist, 1980; Vickery, 1978; Kaden, 1974). Taken together, optical absorption, MCD, and EPR data can form the basis for a detailed spectroscopic analysis of active site metal ions providing greater information than is available from any single technique. This information can be interpreted at levels ranging from the most empirical (number and type of metal centers, ligand affinities) to theoretical analyses that give insight into structure and interactions of the metal complex. Fundamental spectroscopic studies of the latter kind can ultimately give information on biomolecular structures beyond atomic resolution limits of x-ray diffraction studies to reveal a level of electronic structural detail relating directly to chemistry.

A theoretical framework is needed to relate the spectroscopic measurements to important features of the electronic structure, and while simple models are available for understanding the basic features of absorption and EPR spectra for metal complexes, the lack of effective models for computing polarization intensities in low symmetry complexes has largely restricted the interpretation of MCD spectra. Much of the theoretical MCD literature relates to the high symmetry limit for molecular geometry, limiting its utility in studies on low symmetry biological complexes. An approach based on the angular overlap model united atom approach has been applied to MCD spectroscopy (Gerstman and Brill, 1985), assuming degeneracy of states contributing to intensity. This earlier work has contributed to a clearer understanding of the importance of spin orbit mixing for MCD in low symmetry complexes. In this paper we present an alternative ligand field model for computing characteristic patterns of MCD spectra for cupric complexes in arbitrary geometries. This approximate method provides a framework for interpreting MCD spectra of copper metalloenzymes, extending the effectiveness of an important spectroscopic probe.

Received for publication 5 January 1995 and in final form 23 May 1995.

Address reprint requests to Dr. James W. Whittaker, Department of Chemistry, Carnegie Mellon University, 4400 Fifth Ave., Pittsburgh, PA. Tel.: 412–268-5670; Fax: 412–268-6945; E-mail: jim@insight.chem.cmu.edu.

0006-3495/95/08/674/16 $2.00

MATERIALS AND METHODS

Synthetic complexes and enzyme samples were prepared as previously described (Whittaker et al., 1993; Whittaker and Whittaker, 1988). Optical absorption spectra were recorded on a Varian Instruments (Sugarland, TX) Cary 5 UV-vis-near infared (NIR) absorption spectrometer. Magnetic circular dichroism spectra were measured on an AVIV (Lakewood, NJ) Model 41DS UV-vis-NIR CD spectrometer using an Oxford Instruments (Concord, MA) SM4–6T high field (to 6 T) variable temperature (1.5–300 K) magnetocryostat (Whittaker and Whittaker, 1991). For the visible spectrum (300–850 nm) a Hamamatsu (Bridgewater, NJ) photomultiplier tube served as the detector. In the NIR region (800–2000 nm) this was replaced by a liquid nitrogen-cooled InSb photovoltaic photodiode (model J10D; Judson IR, Montgomeryville, PA). Samples for MCD experiments were prepared by sandwiching a 50% aqueous glycerol solution (for proteins) or a mineral oil mull (for synthetic complexes) between quartz disks and cooling slowly to low temperature in the cryostat.

Simulations of the spectral data were performed using the program nu wave (described below) compiled on a Silicon Graphics (Mountain View, CA) Indigo^2 workstation operating with a 150 MHz R4400 processor. Typical benchmark results: simulation of solution spectra averaged over 10 steps for each Euler angle required 20 s of cpu time. A copy of the simulation program nu wave may be obtained from the authors by submitting an E-mail request to jim@insight.chem.cmu.edu.

Background

Optical absorption (ABS), MCD, and EPR spectroscopies are closely related. As shown in Scheme 1, the electronic states of a paramagnetic molecule split in a magnetic field

(the Zeeman interaction), and transitions can be induced among ground state sublevels (EPR spectroscopy). Electronic transitions become polarized in a magnetic field (the Faraday effect, the basis for MCD spectroscopy) according to the selection rules for absorption of circularly polarized light (Scheme 1 *inset*). The relative intensities of left- and right-handed absorption will vary with temperature in a complementary fashion as the thermal populations over the ground state sublevels change. The total absorption (ABS), being the sum over polarizations ($\varepsilon = \varepsilon_L + \varepsilon_R$), is independent of temperature, while MCD, defined as the difference between polarizations ($\Delta\varepsilon = \varepsilon_L - \varepsilon_R$) exhibits dramatic temperature dependence containing information on the Zeeman splittings in the ground state, complementing the information available from EPR experiments. EPR, absorption, and MCD spectral measurements each contribute information on the energy splittings and wavefunctions for molecular electronic states.

LIGAND FIELD THEORY AND THE ELECTRONIC STRUCTURE OF INORGANIC COMPLEXES

Ligand field theory describes the electronic structure of transition metal complexes in terms of an expansion of ligand perturbations in spherical harmonics centered on the metal ion, giving the electronic energies as functions of angular features of the complex (Scheme 2). The choice of coordinate system defining the ligand positions is arbitrary, and the unitary equivalence of all descriptions related by a rotation in the basis space is used in the spectroscopic calculations described below. Ligand field theory serves as a simple model for covalency, the correct description of the ligand perturbation in most coordination complexes (Ballhausen and Gray, 1964), and in its simplest form is a one-electron (one-hole) picture that is particularly suited to d^1 and d^9 metal ions. Simplicity is the main virtue of the theory, allowing metal-ligand interactions to be computed efficiently in the interpretation of electronic spectra (Companion and Komarynsky, 1964; Lever, 1984).

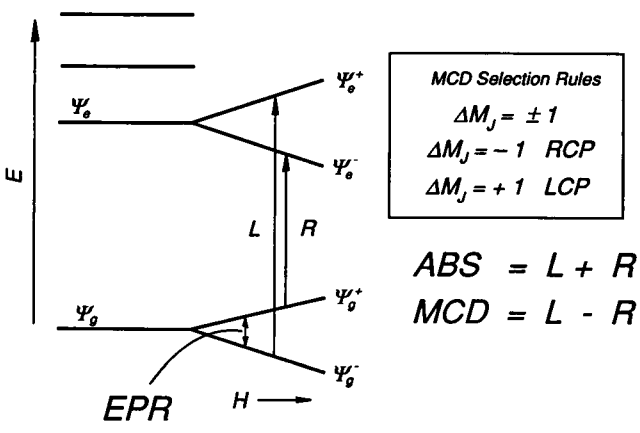

Scheme 1

Conventional ligand field calculations, being restricted to d-orbital functions, fail to account for the intensity of transitions, since d → d spectra are orbitally forbidden (no change in parity) for the electric dipole mechanism. Experimentally, d → d spectra, although weak, are actually observed consistent with mixture of odd parity functions into the d-orbital set through perturbations of the metal complex (Ballhausen, 1962, 1979). Vibrations (in centrosymmetric complexes) or static distortions (in lower symmetry) relax the parity selection rule, mixing even and odd functions and giving intensity to d → d spectra. The odd parity functions most effective in contributing to d → d intensity are associated with low energy (~20,000 cm^{-1}) ligand-to-metal charge transfer (LMCT) excited states that become allowed through covalent mixing of metal and ligand wavefunctions (Ballhausen and Gray, 1964). (Scheme 3) LMCT transitions of σ symmetry, which displace electronic charge along a metal-ligand axis giving them odd (vector displacement) character, tend to be stronger than π LMCT transitions. While absolute intensity calculations for charge transfer-induced spectra must involve integrals over both metal and ligand coordinates, relative intensities can be efficiently calculated by replacing the ligand-centered charge wavefunctions by metal-centered wavefunctions transforming identically, preserving the symmetry of the problem. Although odd parity metal functions (e.g., p- and f-orbitals) lying at relatively high energies in the free ion (>100,000 cm^{-1} (Moore, 1952)) are unlikely to be important for intensity in real metal complexes, they can be used in calculations to mimic the directional covalency that gives intensity to d → d spectra through charge transfer mixing (Ballhausen, 1962). σ LMCT gives rise to states of T_{1u} (vector) symmetry in the octahedral (O_h) point group, and T-P equivalence (Griffith, 1964) justifies expanding the d-orbital basis with odd parity p-orbital functions, while π LMCT states require a linear combination of f wavefunctions for their representation (Scheme 3).

Electronic states arising from configurations involving partly filled subshells (e.g., d^n) can be classified by the number of valence electrons, n, with configurations related as electron-hole complements (e.g., d^n and d^{10-n}) being equivalent up to a sign (Griffith, 1964). These complementary configurations give rise to the same electronic states but in reverse order as expected for the oppositely signed interaction of negative electrons and positive holes. Similarly, σ LMCT for a d^9 cupric ion can be viewed as the hole analog of an interconfiguration d → p transition. Through electron-hole equivalence, d-p mixing calculations for a d^1 metal complex give insight into the LMCT spectra of d^9 metal complexes.

The α parameters that scale the magnitude of the ligand perturbation arise as the radial component in the spherical harmonic expansion of the ligand field Coulomb operator ($1/r$) (Eyring et al., 1944):

$$\alpha_l^i = (Z_i e^2 / a_i^{l+1}) \int R_b r^l R_a r^2 dr$$

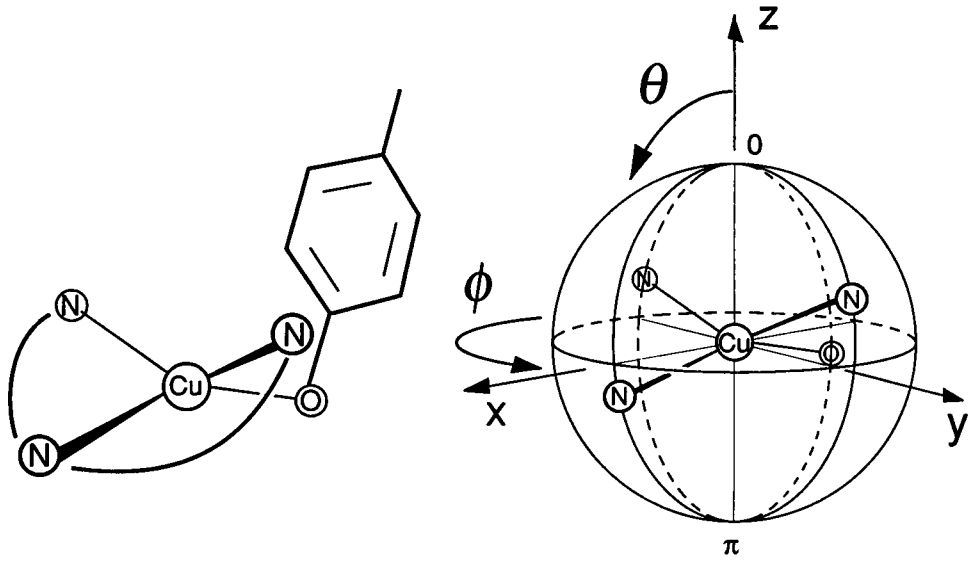

Scheme 2

The α_i^j can be estimated using ligand radial positions a_i and hydrogenic radial wavefunctions R_q (Weissbluth, 1978) incorporating Slater's shielding correction for the Cu^{2+} $3d^9$ ion (Griffith, 1964):

$$R_{3d} = \left(\frac{Z_{eff}}{a_0}\right) 3/2 \left(\frac{4}{81(30)^{1/2}}\right)\left(\frac{Z_{eff}^2 r^3}{a_0^2}\right) \exp\left(\frac{-Z_{eff} r}{3a_0}\right)$$

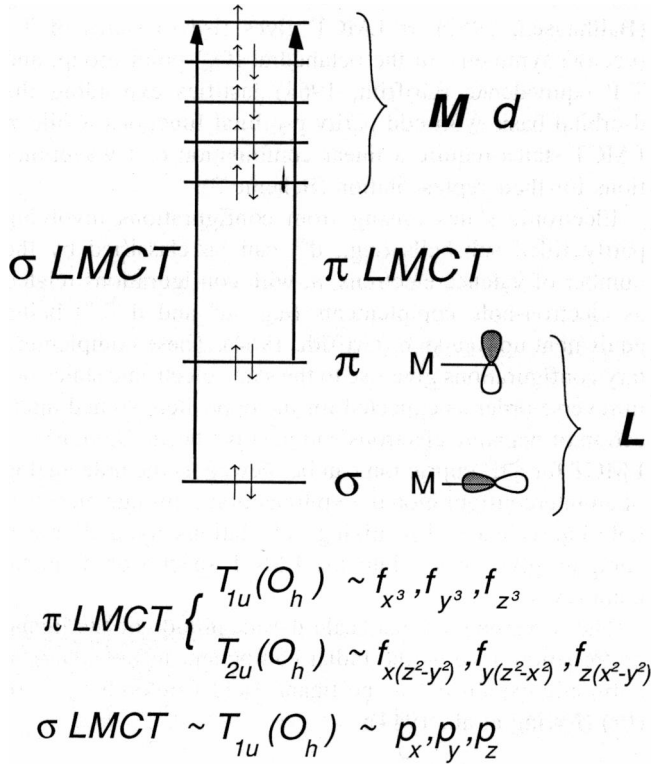

Scheme 3

where the effective nuclear charge Z_{eff} ($Z - \sigma_{Cu^{2+}}$) ~ 8.2, (Z being the nuclear charge and $\sigma_{Cu^{2+}}$ being the Slater shielding factor for the Cu^{2+} ion), a_0 is the Bohr radius (0.528 Å), and r is the radial coordinate. The α_2/α_4 ratio is found to be 3.2, reproducing the generally accepted approximate value ($\alpha_2/\alpha_4 = 3$) (Companion and Komarynsky, 1964). In applications, the α_2/α_4 ratio generally departs significantly from this theoretical value, and the parameters become empirical guides to metal-ligand interaction strength. The d-p mixing parameters can be estimated similarly, using the same procedure as above with approximate 4p radial wavefunctions leading to a theoretical ratio $\alpha_1/\alpha_3 \sim 2$ for d-p mixing. Since excited states important for optical spectra of real metal complexes are not p-orbital states, the α_1/α_3 ratio can be expected to vary in fitting experimental data. Each ligand is parameterized by a set of at least seven of these ligand field parameters (α_0^d, α_2^d, α_4^d, α_0^p, α_2^p, α_1^{dp}, and α_3^{dp}), making a reduction in the number of adjustable parameters desirable. The shift term for the d-orbitals (α_0^d) may be set to zero without loss of generality; and from the principle of spectroscopic stability, p-orbital ligand field splittings may be neglected and the d-p separation may be given an arbitrary value, which serves to remove the d → p transitions from the spectral range of interest.

The ligand field integrals involving d and p orbital wavefunctions are evaluated by summing functions of ligand angular coordinates (D_{lm}, G_{lm}) over all the ligands in the complex to give the complete ligand field contribution to the Hamiltonian in terms of the α parameters. (Companion and Komarynsky, 1964; Lever, 1984). The specific angular functions defining the elementary ligand contributions to the metal perturbation are listed in Tables 1 and 2, in which the d-d matrix elements (Companion and Komarynsky, 1964; Lever, 1984) have been extended to include addi-

TABLE 1 D_{lm} and G_{lm} factors for ligand field multipole calculation

d-d terms

$D^i_{00} = \alpha^i_0\ (d)$
$D^i_{20} = \alpha^i_2\ (d)\ (3\cos^2\theta_i - 1)$
$D^i_{40} = \alpha^i_4\ (d)\ (35/3\ \cos^4\theta_i - 10\ \cos^2\theta_i + 1)$
$D^i_{21} = \alpha^i_2\ (d)\ (\sin\theta_i\ \cos\theta_i\ \cos\phi_i)$
$D^i_{22} = \alpha^i_2\ (d)\ (\sin^2\theta_i\ \cos2\phi_i)$
$D^i_{41} = \alpha^i_4\ (d)\ (\sin\theta_i\ \cos\theta_i(7/3\ \cos^2\theta_i - 1)\cos\phi_i)$
$D_{42i} = \alpha^i_4\ (d)\ (\sin^2\theta_i(7\cos^2\theta_i - 1)\cos2\phi_i)$
$D^i_{43} = \alpha^i_4\ (d)\ (\sin^3\theta_i\ \cos\theta_i\ \cos3\phi_i)$
$D^i_{44} = \alpha^i_4\ (d)\ (\sin^4\theta_i\ \cos4\phi_i)$
$G^i_{21} = \alpha^i_2\ (d)\ (\sin\theta_i\ \cos\theta_i\ \sin\phi_i)$
$G^i_{22} = \alpha^i_2\ (d)\ (\sin^2\theta_i\ \sin2\phi_i)$
$G^i_{41} = \alpha^i_4\ (d)\ (\sin\theta_i\ \cos\theta_i(7/3\ \cos^2\theta_i - 1)\sin\phi_i)$
$G^i_{42} = \alpha^i_4\ (d)\ (\sin^2\theta_i(7\cos^2\theta_i - 1)\sin2\phi_i)$
$G^i_{43} = \alpha^i_4\ (d)\ (\sin^3\theta_i\ \cos\theta_i\ \sin3\phi_i)$
$G^i_{44} = \alpha^i_4\ (d)\ (\sin^4\theta_i\ \sin4\phi_i)$

p-p terms

$D^i_{00} = \alpha^i_0\ (p)$
$D^i_{20} = \alpha^i_2\ (p)\ (3\cos^2\theta_i - 1)$
$D^i_{40} = \alpha^i_4\ (p)\ (35/3\ \cos^4\theta_i - \cos^2\theta_i + 1)$
$D^i_{21} = \alpha^i_2\ (p)\ (\sin\theta_i\ \cos\theta_i\ \cos\phi_i)$
$D^i_{22} = \alpha^i_2\ (p)\ (\sin^2\theta_i\ \cos2\phi_i)$
$G^i_{21} = \alpha^i_2\ (p)\ (\sin\theta_i\ \cos\theta_i\ \sin\phi_i)$
$G^i_{22} = \alpha^i_2\ (p)\ (\sin^2\theta_i\ \sin2\phi_i)$

d-p terms

$D^i_{10} = \alpha^i_1\ (\cos\theta_i)$
$D^i_{30} = \alpha^i_3\ (\cos\theta_i(5/3\ \cos^2\theta_i - 1))$
$D^i_{11} = \alpha^i_1\ (\sin\theta_i\ \cos\phi_i)$
$D^i_{31} = \alpha^i_3\ (\sin\theta_i(5\ \cos^2\theta_i - 1)\cos\phi_i)$
$D^i_{32} = \alpha^i_3\ (\sin^2\theta_i\ \cos\theta_i\ \cos2\phi_i)$
$D^i_{33} = \alpha^i_3\ (\sin^3\theta_i\ \cos3\phi_i)$
$G^i_{11} = \alpha^i_1\ (\sin\theta_i\ \sin\phi_i)$
$G^i_{31} = \alpha^i_3\ (\sin\theta_i(5\ \cos^2\theta_i - 1)\sin\phi_i)$
$G^i_{32} = \alpha^i_3\ (\sin^2\theta_i\ \cos\theta_i\ \sin2\phi_i)$
$G^i_{33} = \alpha^i_3\ (\sin^3\theta_i\ \sin3\phi_i)$

d-f terms

$D^i_{10} = \alpha^i_1\ (\cos\theta_i)$
$D^i_{30} = \alpha^i_3\ (\cos\theta_i(5/3\ \cos^2\theta_i - 1))$
$D^i_{11} = \alpha^i_1\ (\sin\theta_i\ \cos\phi_i)$
$D^i_{31} = \alpha^i_3\ (\sin\theta_i(5\ \cos^2\theta_i - 1)\cos\phi_i)$
$D^i_{32} = \alpha^i_3\ (\sin^2\theta_i\ \cos\theta_i\ \cos2\phi_i)$
$D^i_{33} = \alpha^i_3\ (\sin^3\theta_i\ \cos3\phi_i)$
$D^i_{50} = \alpha^i_5\ (\cos\theta_i - 70/15\ \cos^3\theta_i + 60/15\cos^5\theta_i)$
$D^i_{51} = \alpha^i_5\ ((14\ \cos^2\theta_i\ \sin\theta_i - \sin\theta_i - 21\cos^4\theta_i\ \sin\theta_i)\cos\phi_i)$
$D^i_{52} = \alpha^i_5\ (\sin^2\theta_i(\cos^3\theta_i - \cos\theta_i)\cos2\phi_i)$
$D^i_{53} = \alpha^i_5\ (1 - 9\ \cos^2\theta_i)\ \sin^3\theta_i\ \cos3\phi_i)$
$D^i_{54} = \alpha^i_5\ (\cos\theta_i\ \sin^4\theta_i\ \cos4\phi_i)$
$D^i_{55} = \alpha^i_5\ (\sin^5\theta_i\ \cos5\phi_i)$
$G^i_{11} = \alpha^i_1\ (\sin^2\theta_i\ \sin\phi_i)$
$G^i_{31} = \alpha^i_3\ (\sin\theta_i(5\ \cos^2\theta_i - 1)\sin\phi_i)$
$G^i_{32} = \alpha^i_3\ (\sin^2\theta_i\ \cos\theta_i\ \sin2\phi_i)$
$G^i_{33} = \alpha^i_3\ (\sin^3\theta_i\ \sin3\phi_i)$
$G^i_{51} = \alpha^i_5\ (\sin\theta_i(-21\ \cos^4\theta_i + 14\ \cos^2\theta_i - 1)\sin\phi_i)$
$G^i_{52} = \alpha^i_5\ (\sin^2\theta_i(\cos^3\theta_i - \cos\theta_i)\sin2\phi_i)$
$G^i_{53} = \alpha^i_5\ ((1 - 9\ \cos^2\theta_i)\ \sin^3\theta_i\ \sin3\phi_i)$
$G^i_{54} = \alpha^i_5\ (\sin^4\theta_i\ \cos\theta_i\ \sin4\phi_i)$
$G^i_{55} = \alpha^i_5\ (\sin^5\theta_i\ \sin5\phi_i)$

tional p-p, d-p, and d-f matrix elements. The Hamiltonian matrix H_{ij} is indexed as follows:

$$(i = 1 - 5)(d^+_{x^2-y^2}\ d^+_{xz}\ d^+_{z^2}\ d^+_{yz}\ d^+_{xy})(i = 6 - 10)$$

$$(d^-_{x^2-y^2}\ d^-_{xz}\ d^-_{z^2}\ d^-_{yz}\ d^-_{xy})(i = 11 - 13)(p^+_x\ p^+_z\ p^+_y)$$

$$(i = 14 - 16)(p_x\ p^-_z\ p^-_y)$$

for the σ LMCT model, where the sign indicates spin up (+) or spin down (−).

The complete Hamiltonian, composed of three parts (the ligand field Hamiltonian (discussed above), spin orbit coupling, and the Zeeman perturbation) can be represented by a 16 × 16 matrix, blocked out into d and p submatrices, spin up and spin down for each as illustrated in Scheme 4. Nonvanishing matrix elements are shaded in Scheme 4 to emphasize the pattern of each of the perturbation terms. The ligand field ($\mathcal{H}_{LF}$) is diagonal in the real d-orbital basis set, angular momentum being quenched through orbital splittings (Van Vleck, 1932) that are detected in d → d spectra. The p orbital set also splits, and for a complex lacking a center of symmetry (e.g., square pyramidal geometry), d-p mixing occurs as a consequence of nonvanishing elements in the off-diagonal blocks that arise through odd components (Y^m_1 and Y^m_3) of the ligand field providing the intensity mechanism for d → d transitions. Spin orbit coupling ($\mathcal{H}_{SO}$) is purely off-diagonal in this scheme, mixing orbital functions and unquenching orbital momentum, a mechanism for MCD intensity and for orbital g-shifts (deviations from the free-electron g value, $g_e = 2.0023$) in EPR spectra. For a molecule in a magnetic field, the Zeeman perturbation ($\mathcal{H}_{Zee}$) is mixed diagonal and off-diagonal, splitting and mixing levels, giving rise to EPR transitions and temperature-dependent MCD spectra. Diagonalizing the complete Hamiltonian yields eigenvalues and eigenvectors from which the spectra are computed.

The Theory of the Absorption Coefficient

Electric dipole contributions to intensity are intrinsically more than five orders of magnitude stronger than the next most important term (Ballhausen, 1979), so that even a small fraction of electric dipole character mixed into a transition dominates the intensity mechanism. The present model calculates intensity in terms of electric dipole matrix elements using the transition vector operator ($\mathbf{m} = e\mathbf{r}$), which contains both a linear displacement (Δr) and polarization (angular orientation) component. The displacement term defines the absolute intensity scale for the spectra, and the polarization terms can be evaluated as Gaunt coefficients, angular integrals over triple products of spherical harmonics (Gaunt, 1929). In applying selection rules, the lab-fixed transition operators (M_x, M_y, M_z) may be replaced by real combinations of spherical harmonics transforming identically, the vector operator equivalents:

$$M_x = V_x = \frac{1}{2^{1/2}}(V_{-1} - V_{+1}) \sim \frac{1}{2^{1/2}}(Y^{-1}_1 - Y^{+1}_1),\ M_y = V_y$$

$$= \frac{i}{2^{1/2}}(V_{-1} + V_{+1}) \sim \frac{i}{2^{1/2}}(Y^{-1}_1 + Y^{+1}_1),\ M_z = V_z \sim Y^0_1$$

(Piepho and Schatz, 1983). Similarly, MCD intensity is computed using the lab-fixed right- and left-hand transition operators M_{-1} and M_{+1} (represented respectively by their

TABLE 2 Ligand field Hamiltonian matrix elements H_{pq}

d-d	
H^i_{11} =	$D^i_{00} - 0.14286\,D^i_{20} + 0.01785\,D^i_{40} + 0.20833\,D^i_{44}$
H^i_{12} = 0.42857	$D^i_{21} - 0.17857\,D^i_{41} + 0.41667\,D^i_{43}$
H^i_{13} = −0.24744	$D^i_{22} + 0.10310\,D^i_{42}$
H^i_{14} = −0.42857	$G^i_{21} + 0.17857\,G^i_{41} + 0.41667\,G^i_{43}$
H^i_{15} = 0.20833	G^i_{44}
H^i_{22} =	$D^i_{00} + 0.07142\,D^i_{20} - 0.07142\,D^i_{40} + 0.21428\,D^i_{22} + 0.11904\,D^i_{42}$
H^i_{23} = 0.24743	$D^i_{21} + 0.61860\,D^i_{41}$
H^i_{24} = 0.21428	$G^i_{22} + 0.11905\,G^i_{42}$
H^i_{25} = 0.42857	$G^i_{21} - 0.17857\,G^i_{41} + 0.41667\,G^i_{43}$
H^i_{33} =	$D^i_{00} + 0.14285\,D^i_{20} + 0.10714\,D^i_{40}$
H^i_{34} = 0.24743	$G^i_{21} + 0.61860\,G^i_{41}$
H^i_{35} = −0.24744	$G^i_{22} + 0.10310\,G^i_{42}$
H^i_{44} =	$D^i_{00} + 0.07142\,D^i_{20} - 0.07142\,D^i_{40} - 0.21428\,D^i_{22} - 0.11904\,D^i_{42}$
H^i_{45} = 0.42857	$D^i_{21} - 0.17857\,D^i_{41} - 0.41667\,D^i_{43}$
H^i_{55} =	$D^i_{00} - 0.14285\,D^i_{20} + 0.01785\,D^i_{40} - 0.20833\,D^i_{44}$
p-p	
$H_{11\,11}$ =	$D^i_{00} - 0.10000\,D^i_{20} + 0.30000\,D^i_{22}$
$H_{11\,12}$ = 0.60000	D^i_{21}
$H_{11\,13}$ = 0.30000	G^i_{22}
$H_{12\,12}$ =	$D^i_{00} + 0.20000\,D^i_{20}$
$H_{12\,13}$ = 0.60000	G^i_{21}
$H_{13\,13}$ =	$D^i_{00} - 0.10000\,D^i_{20} - 0.30000\,D^i_{22}$
d-p	
$H_{1\,11}$ = 0.4472	$D^i_{11} - 0.0479\,D^i_{31} + 0.2395\,D^i_{33}$
$H_{1\,12}$ = 0.4792	D^i_{32}
$H_{1\,13}$ = −0.4472	$G^i_{11} + 0.0479\,G^i_{31} + 0.2395\,G^i_{33}$
$H_{2\,11}$ = 0.44718	$D^i_{10} - 0.2874\,D^i_{30} + 0.4792\,D^i_{32}$
$H_{2\,12}$ = 0.44718	$D^i_{11} + 0.1915\,D^i_{31}$
$H_{2\,13}$ = 0.4792	G^i_{32}
$H_{3\,11}$ = 0.2582	$D^i_{11} + 0.1659\,D^i_{31}$
$H_{3\,12}$ = 0.5157	$D^i_{10} + 0.4980\,D^i_{30}$
$H_{3\,13}$ = −0.2582	$G^i_{11} + 0.1659\,G^i_{31}$
$H_{4\,11}$ = 0.4792	G^i_{32}
$H_{4\,12}$ = 0.44718	$G^i_{11} + 0.1917\,G^i_{31}$
$H_{4\,13}$ = 0.44718	$D^i_{10} - 0.287\,D^i_{30} - 0.4792\,D^i_{32}$
$H_{5\,11}$ = 0.44718	$G^i_{11} - 0.0479\,G^i_{31} + 0.2395\,G^i_{33}$
$H_{5\,12}$ =0.479	G^i_{32}
$H_{5\,13}$ = 0.4472	$D^i_{11} - 0.0479\,D^i_{31} - 0.2395\,D^i_{33}$
d-f	
$H_{1\,16}$ = 0.18898	$D^i_{11} + 0.04725\,D^i_{31} - 0.07874\,D^i_{33} - .02147\,D^i_{51} + 0.06264\,D^i_{53} + 0.11275\,D^i_{55}$
$H_{1\,17}$ = −0.18898	$G^i_{11} - 0.04725\,G^i_{31} - 0.07874\,G^i_{33} + .02147\,G^i_{51} + 0.06264\,G^i_{53} - 0.11275\,G^i_{55}$
$H_{1\,18}$ = 0.37796	$D^i_{10} - 0.12599\,D^i_{30} + 0.10738\,D^i_{50} + 0.45098\,D^i_{54}$
$H_{2\,16}$ = 0.37796	$D^i_{10} + 0.031497\,D^i_{30} + .47245\,D^i_{32} - 0.26844\,D^i_{50} + 0.30065\,D^i_{52} + 0.22549\,D^i_{54}$
$H_{2\,17}$ = 0.45098	$G^i_{52} - 0.22549\,G^i_{54}$
$H_{2\,18}$ = 0.37796	$D^i_{11} + 0.09449\,D^i_{31} + 0.15748\,D^i_{33} - 0.04295\,D^i_{51} + 0.10022\,D^i_{53}$
$H_{3\,16}$ = 0.32733	$D^i_{11} + 0.818317\,D^i_{31} + 0.13639\,D^i_{33} + 0.09299\,D^i_{51} + 0.043397\,D_{53}{}^i$
$H_{3\,17}$ = 0.32732	$G^i_{11} + 0.08183\,G^i_{31} + 0.13639\,G^i_{33} + .09299\,G^i_{51} - 0.04340\,G^i_{53}$
$H_{3\,18}$ = 0.52075	D^i_{52}
$H_{4\,16}$ = 0.45098	$G^i_{52} + 0.22549\,G^i_{54}$
$H_{4\,17}$ = 0.53452	$D^i_{10} + 0.06299\,D^i_{30} - 0.47245\,D^i_{32} - 0.53688\,D^i_{50} - 0.30065\,D^i_{52} + 0.22549\,D^i_{54}$
$H_{4\,18}$ = 0.37796	$G^i_{11} - 0.09449\,G^i_{31} + 0.15748\,G^i_{33} + 0.04295\,G^i_{51} + 0.10022\,G^i_{53} - 0.37796$
$H_{5\,16}$ = −0.37796	$G^i_{11} + 0.14174\,G^i_{31} - 0.07874\,G^i_{33} - 0.032213\,G^i_{51} + 0.062636\,G^i_{53} + 0.11274\,G^i_{55}$
$H_{5\,17}$ = −0.37796	$D^i_{11} + 0.14174\,D^i_{31} + 0.07874\,D^i_{33} - 0.032213\,D^i_{51} - 0.062636\,D^i_{53} + 0.11274\,D^i_{55}$
$H_{5\,18}$ = 0.45098	G^i_{54}

vector operator equivalents, $V_{-1}{\sim}Y_1{}^{-1}$ and $V_{+1}{\sim}Y_1{}^{+1}$) between each pair of eigenvectors that includes one component of the ground doublet. The circular polarization operators transform respectively like $\mathbf{X} + i\mathbf{Y}$ (right circularly polarized, RCP) and $\mathbf{X} - i\mathbf{Y}$ (left circularly polarized, LCP) corresponding to photons in pure angular momentum states, with angular momentum directed antiparallel (−1) and parallel (+1) to the propagation vector, **k** (Scheme 5). The conservation of angular momentum when a molecule absorbs a circularly polarized photon carrying intrinsic angular momentum (±1) determines the selection rules for MCD (Scheme 1, *inset*). Circularly polarized photon helicity states are also chiral, and interactions of a chiral absorber with right- and left-hand circularly polarized photons are

$$\mathcal{H} = \mathcal{H}_{LF} + \mathcal{H}_{SO} + \mathcal{H}_{ZEE}$$

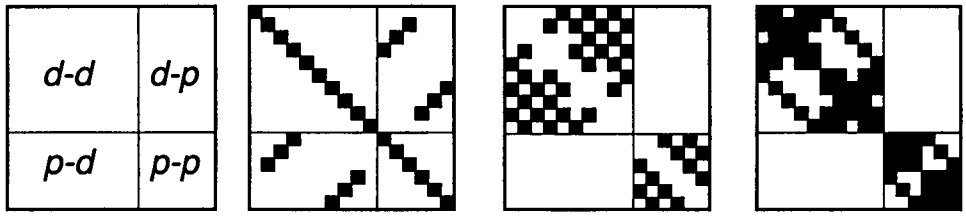

Scheme 4

diastereomeric, eliminating the symmetry between absorption coefficients for right- and left-handed light. This is the basis of natural CD, which depends on the chirality of circularly polarized light, while MCD depends on the fact that circularly polarized light carries angular momentum.

The ligand field calculations are performed in a d-, p-, and f- basis referred to the magnetic field (laboratory Z-) direction rather than the molecular axes so that the resulting molecular electronic wavefunctions are formed from angular momentum functions diagonal in the Zeeman interaction as required for computing MCD intensity. Formulating the calculation in the lab frame makes it necessary to reevaluate all ligand field matrix elements in the rotated frame during orientation averaging to simulate solution spectra, but the evaluation of transition integrals is reduced to summing a set of Gaunt coefficients that can be stored efficiently in a subroutine. This use of lab-fixed frame in the calculation is motivated by the basic geometry of the MCD experiment, where the light propagates longitudinally through the magnetic field and the oscillating radiation electric fields ($\mathbf{E}_x$, $\mathbf{E}_y$) that induce transitions are always transverse to the magnetic field direction (Scheme 5).

Eq. 1 relates molecular properties (transition dipole amplitude) to spectroscopic measurements, providing the correct normalization for the transition intensity (Piepho and Schatz, 1983):

$$A = \frac{1}{2}\gamma E(|<\Psi_g|M_{-1}|\Psi_e>|^2 + |<\Psi_g|M_{+1}|\Psi_e>|^2) \quad (1)$$

where E is the transition energy, M is the complex electric dipole transition operator and

$$\gamma = (N_A\pi^3\alpha^2\log_{10}e/125hcn)$$

where N_A is Avagadro's number, $\alpha = (n^2 + 2)/3$, h is Planck's constant, c is the velocity of light in vacuo, n is the refractive index, and the factor of 2 arises from the resolution of unpolarized light into equal parts of right and left polarized components. For MCD, the corresponding relation is

$$\Delta A = \gamma E(|<\Psi_g|M_{-1}|\Psi_e>|^2 - |<\Psi_g|M_{+1}|\Psi_e>|^2) \quad (2)$$

where ΔA is the total MCD intensity. The total MCD is conventionally resolved into Faraday components: a diamagnetic A Term, paramagnetic C term, and a B term describing Zeeman mixing among zero field states. The A term corresponds to the high temperature limit of MCD intensity, when both sublevels of the ground doublet (Scheme 1) are equally populated, and the right and left transitions (contributing to negatively and positively signed intensity, respectively, in MCD) being equal in magnitude and oppositely signed nearly cancel except for a small Zeeman shift in the transition energies ($\Delta E \sim 10\ cm^{-1}$), which results in a weak temperature-independent derivative-shaped signal. At lower temperatures, the upper sublevel is depopulated leading to a dramatic (~100-fold) increase in intensity. The resulting signal has an absorption bandshape, exhibits a Curie Law reciprocal temperature dependence, and is known as an MCD C term. The C Term signal saturates at low temperature and exhibits a magnetization behavior that gives information on ground state g values (Schatz et al., 1978; Johnson and Thomson, 1980). The relative intensities of A, B, and C terms are proportional to the reciprocal linewidth ($1/\Gamma$) the energy splitting between zero field states ($1/\Delta E$) and the thermal energy (1/kT), respectively. Typical values of these parameters ($\Gamma = 1000\ cm^{-1}$, $\Delta E = 10{,}000\ cm^{-1}$, $kT = 10\ cm^{-1}$) leads to a predicted 1: 0.1: 100 ratio for A, B, and C terms at low temperature. The low temperature spectrum is therefore dominated by the paramagnetic C term MCD signal that comes from MCD arising from the lowest sublevel in the ground state. By computing the total MCD, these calculations automatically include all three terms, and the C and A terms can be evaluated as the low and infinite temperature limit in our model. The Faraday $\mathscr{C}$ and $\mathscr{D}$ parameters for C Term MCD intensity and total absorption are related to the absorptivities (A) and differential absorptivities (ΔA) above:

$$\Delta A(H,T) = \gamma \mathscr{C}_0(\beta H/2kT) \quad (3)$$

$$A = \gamma \mathscr{D}_0 \quad (4)$$

and can be straightforwardly evaluated from the calculations.

The simulation of MCD spectra involves evaluation of spectroscopic transition probabilities by summing appropriately indexed Gaunt coefficients ($<i|M_q|j>$, $q = \pm 1$) multiplied by products of complex eigenvector coefficients for ground and excited state electronic wavefunctions:

$$\Delta A = \gamma\{|[\sum_{ij} c_i^* c_j <i|M_{-1}|j>]|^2 - |[\sum_{ij} c_i^* c_j <i|M_{+1}|j>]|^2\} \quad (5)$$

where i and j index the eigenvector basis components of the ground and excited orbital states, c_i and c_j being the eigenvector coefficients. This calculation is repeated for both the lower and upper sublevels of the ground doublet, the intensity from each being weighted by the Boltzmann factor appropriate for the ground state at the assigned temperature and magnetic field strength. These intensities are written to a transition array, which is numerically integrated over angles to achieve the orientationally averaged result corresponding to a solution spectrum (see below). Alternatively, the spectra may be computed for any arbitrary single orientation of the complex, to display the individual oriented spectra from which the solution result is composed. The stick spectra obtained by this calculation are then convoluted with a Gaussian absorption lineshape

$$f(\nu) = \left(\frac{1}{\sigma\sqrt{2\pi}}\right)\exp\left(\frac{-(E-E_0)^2}{2\sigma^2}\right) \quad (6)$$

where the full width at half maximum (Γ_{FWHM}) for the absorption band is taken to be $\sigma(2\ln 2)^{1/2}$.

Orientation averaging is achieved by numerical evaluation of the angular integral (Eq. 7) using a modified Simpson's Rule integration algorithm (Press et al., 1992) over the three Euler angles θ, χ, and ϕ:

$$\Delta\epsilon = \gamma\frac{1}{8\pi^2}\int_{\phi=0}^{2\pi}\int_{\chi=0}^{2\pi}\int_{\theta=0}^{\pi}\Delta A(\theta,\chi,\phi)\sin\theta d\theta d\chi d\phi \quad (7)$$

Since the magnetic field direction defining the laboratory Z axis is fixed in space, a rotation matrix parameterized by Euler angles (Zare, 1988) is applied to the ligand position coordinates and the ligand field Hamiltonian is reevaluated in the new orientation before computing left- and right-polarized intensities in each transition. While the eigenvalues are unchanged by the coordinate rotation, the eigenvectors are transformed leading to a unitarily equivalent redefinition of molecular wavefunctions in terms of the laboratory frame, so that the underlying basis is diagonal in $\mathcal{H}_{Zee}$, described by angular momentum wavefunctions referred to the magnetic field direction.

Complementarity rule for CD and MCD

Natural CD involves interference between electric and magnetic transition dipoles, associated with the transition operator $\mu\cdot\mathbf{m}$, the dot product of an axial vector (μ, the magnetic dipole moment operator) and polar vector ($\mathbf{m}$). This product is a pseudoscalar, distinguished from a scalar by the change of sign it experiences on inversion. A pseudoscalar quantity is not required to cancel upon averaging over orientations, and this leads to a nonvanishing solution CD intensity. On the other hand, MCD is the product of two axial vectors, μ and the vector product ($\mathbf{m}\times\mathbf{m}$). This product is a simple scalar and will not survive full rotational averaging, requiring MCD to vanish. In practice, MCD does not vanish because even for solution spectra the intensity is only partly averaged, over the orientations of the components of the electric dipole moments, while the other component (μ) is fixed in the laboratory. Reversing the direction of the magnetic field relative to the radiation electric field vectors would reverse the sign of the MCD, leading to a cancellation of the spectra.

Empirically, optical transitions that are relatively strong in CD as a general rule appear relatively weak in MCD. On the basis of the analysis outlined above, this rule can be understood as an expression of the distribution of orbital angular momentum over electronic states (Scheme 6). A transition between a pair of levels spanned by a component of orbital angular momentum will be allowed under magnetic dipole selection rules. This contribution to the transition, being relatively weak, will not significantly increase the electric dipole-dominated optical absorption intensity, but will result in a relatively large CD anisotropy ($\Delta\epsilon/\epsilon$). In contrast, the origin of MCD intensity lies in spin-orbit mixing (Piepho and Schatz, 1983; Gerstman and Brill, 1985), which will be most effective when the pair of states involved are nearly degenerate in energy and are spanned by a rotation, implying a component of unquenched orbital momentum. Since the optical transitions occur to levels far removed from the ground state, these two classes of transitions are by necessity mutually exclusive. This can be recognized as a general complementarity principle for polarization spectra: as a consequence of selection rules, transitions that appear strong in CD can be expected to be weak in MCD and vice versa. This rule can be useful in interpreting experimental spectra and as the basis for spectroscopic assignments.

EPR spectra

In contrast to MCD spectra, which contain information on changes in angular momentum between ground and excited

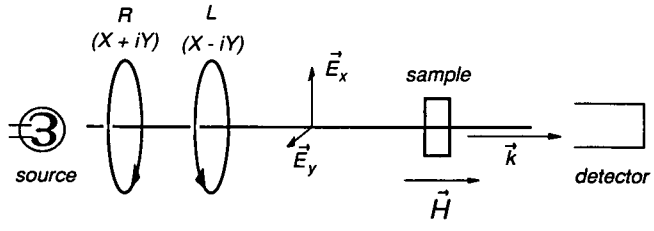

Scheme 5

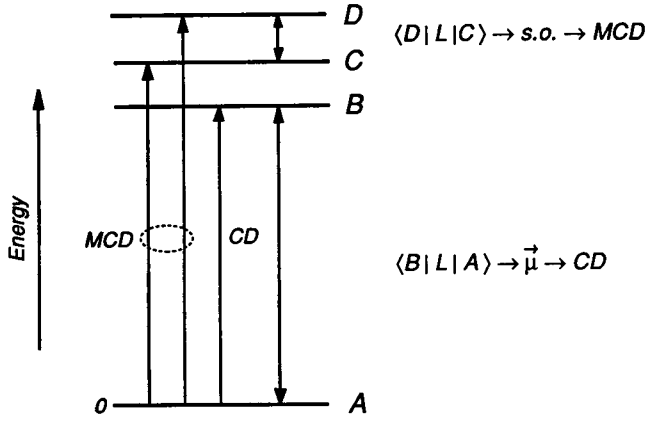

Scheme 6

electronic states, EPR spectra specifically reveal the unquenched orbital momentum in the electronic ground state. The ground state Zeeman energy determines the magnetic field splitting in the ground state, and EPR transitions within the Zeeman-split ground doublet for a spin-1/2 complex are characterized by the magnitude of the g value:

$$\Delta E = \left(< + \frac{1}{2} \left| L + g_e S \right| + \frac{1}{2} > - < - \frac{1}{2} \left| L + g_e S \right| - \frac{1}{2} > \right) \beta H = g \beta H \quad (8)$$

The spin-only splitting is described by the free electron g value, $g_e = 2.0023$. Orbital contributions require an unquenched component of orbital momentum in the ground state associated with a nonvanishing orbital angular momentum matrix element. Deviations from the free electron g value (orbital g shifts) contain information on the nature of the ground state orbital wavefunction. Anisotropy of the Zeeman splitting within the ground doublet results from the spatial orientation of orbital wavefunctions and leads to an orientation dependence of the resonance magnetic field for an EPR transition. The resonance field H_{res} may be computed from the fixed microwave photon energy (0.3 cm^{-1} at X band) and the Zeeman splitting factor g: $H_{res} = h\nu/g\beta$. Neglecting angular dependence of the transition probability that is associated with g-anisotropy, powder spectra can be generated by solving the resonance condition at each point in the orientation averaging grid, convoluting with a lineshape function, and summing over orientations with the $\left(\frac{1}{8\pi^2} sin\theta\right)$ statistical normalization. Forward difference numerical differentiation of the resulting absorption envelope generates the conventional derivative EPR display.

Greater angular resolution is required in simulating EPR spectra than either absorption or MCD to produce a smooth derivative spectrum.

CHARACTERISTIC MCD SPECTRA FOR LIMITING GEOMETRIES

Cubic complexes: the sign of the MCD C term

Applying these approaches to calculating the magnitude and sign of MCD in a d → p transition gives results that can be compared with results of a group theoretical analysis as a test of the model. For a d^1 ion in octahedral symmetry the d → p transition corresponds to a $^2T_{2g} \rightarrow {}^2T_{1u}$ excitation from a $d(t_{2g})^1$ ground state electron configuration to an excited $p(t_{1u})^1$ orbital occupation. Both the ground and excited electronic states are orbitally degenerate, split by the orbital Zeeman interaction in an applied magnetic field. Initial and final states are also both pure angular momentum states, and as a consequence, the transition occurs in pure left polarization according to the selection rules for absorption of circularly polarized light (Scheme 1). The degree of polarization of the transition is described by the anisotropy ($\Delta\varepsilon/\varepsilon$) or as the ratio of Faraday parameters ($\mathscr{C}_o/\mathscr{D}_o$). Since the transition is pure left polarized, $\mathscr{C}_o/\mathscr{D}_o = +1$. The sign and magnitude of the C term MCD intensity has been rigorously evaluated from group theoretical symmetry arguments alone (Stephens, 1965), and the results of the model calculation are in full agreement. This predicts positively signed MCD will dominate the spectra of complexes in the cubic limit but neglects the contributions from $^2T_{2g} \rightarrow {}^2T_{2u}$ transitions that arise in π LMCT and are predicted to contribute negatively signed intensity in MCD (Stephens, 1965). The latter transition cannot be reproduced in the d-p ligand field model, as discussed further below. For a d^9 cupric ion in octahedral coordination, the hole equivalent scheme leads to a $^2E_g \rightarrow {}^2T_{1u}$ description of σ LMCT in this complex. Stephens (1976) has shown using group theory that MCD is allowed in both polarizations for this transition, leading to an A term MCD signature. For a cupric ion in a tetrahedral complex, the corresponding d → p excitation gives rise to a $^2T_2 \rightarrow {}^2T_1$ transition, the parity labels (u,g) being dropped for the noncentrosymmetric complex. The sign of the MCD signal for the d → p transition in the absence of spin orbit coupling is the same as for the $^2T_{2g} \rightarrow {}^2T_{1u}$ transition for the d^1 O_h complex.

For studies on metalloenzymes the geometric structures arising in five-coordination are of particular interest. These include limiting tetragonal, square pyramid, and trigonal bipyramid complexes, as well as lower symmetry structures that may be regarded as intermediates in a distortion between the two limits along the pseudorotation coordinate (Fig. 1) (Berry, 1960; Muertterties and Guggenberger, 1974).

Square pyramid

The square pyramidal (SP) limiting geometry is an idealization of many common five-coordinate cupric complexes. Four equatorial ligands dominate interactions, and a distortion that weakens the axial ligand interactions is typical.

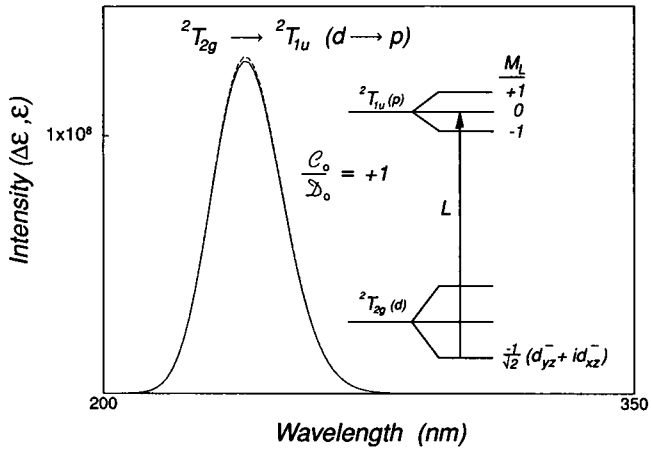

FIGURE 1 Absorption and MCD spectra computed for an octahedral $^2T_{2g} \rightarrow {}^2T_{1u}$ transition. Absorption (——) and MCD (——) spectra calculated for d → p interconfiguration transition for $H/T = k/\beta$. Coincidence of the spectra implies the ratio of Faraday parameters as shown.

Simple ligand field theory predicts a $d_{x^2-y^2}$ orbital ground state for this noncentrosymmetric complex, and for the d^9 cupric ion, the highest energy ligand field state is the orbitally degenerate (d_{xz}, d_{yz}). By symmetry, odd parity ligand field mixing into each of the degenerate orbital components is equal in magnitude. Spin orbit mixing among these orbitals, which contain an unquenched component of angular momentum ($L_z = 1$), leads to the appearance of a pair of MCD signals of equal magnitude and opposite sign, overlapping to form a derivative-shaped feature (pseudo-A term), the MCD sign and intensity reflecting the change in orbital momentum along the magnetic field direction in the transition. EPR predicted for the square pyramidal complex reflects the nature of the ground state wavefunction in the $g_\| > g_\perp > 2$ axial spectrum characteristic of a $d_{x^2-y^2}$ orbital ground state.

Trigonal bipyramid

In the trigonal bipyramidal (TBP) limiting geometry, two ligands interact with the metal ion in axial sites, while three others interact equatorially in a plane equilateral triangle. This ligand arrangement leads to an orbitally nondegenerate ground state of d_{z^2} character. The two orbitally degenerate ligand field excited states each retain unquenched orbital momentum that leads to spin orbit mixing among the levels; however, only the ($d_{x^2-y^2}$, d_{xy}) orbital doublet acquires intensity through mixture of odd functions (see below). EPR computed for the trigonal geometry represents an axial spectrum with $g_\perp > g_\| = 2$ characteristic of the d_{z^2} orbital ground state wavefunction.

Intermediate geometries

The C_{2v} pseudorotation coordinate connects the square and trigonal limiting geometries for a five-coordinate ML_5 metal complex correlating through intermediate geometries that preserve both a twofold rotation axis and a mirror plane. Spectra calculated for a range of geometries between the square and trigonal limits of the pseudorotation coordinate are presented in Fig. 1. The parameters used for the square and trigonal geometries are listed in the figure legend, and the parameters for intermediate geometries are obtained by linear interpolation between these limiting values. These spectra confirm the intuitive expectation that MCD spectra should reflect the approximate symmetry of a complex in that the computed spectra near the high-symmetry limits closely resemble the spectra for the limiting geometries. The calculation also emphasizes that spectra smoothly correlate with geometry for intermediate structures along this distortion coordinate. The variation of EPR spectra from $g_\| > g_\perp > 2$ axial spectrum characteristic of a $d_{x^2-y^2}$ orbital ground state for the square pyramidal complex to the reversed $g_\perp > g_\| = 2$ spectrum characteristic of the d_{z^2} orbital ground state wavefunction for the trigonal bipyramidal complex is well known as a basis for interpreting EPR spectra of cupric complexes. The present ligand field analysis demonstrates that similar characteristic features occur in MCD spectra that permit immediate recognition of essential geometric structural features of a cupric complex from the pattern of MCD intensity.

Intensity mixing and origins of MCD spectra

The mixing of even and odd parity functions in these complexes is determined by the symmetry properties of the orbital wavefunctions. In C_{4v} symmetry, the orbital doublets p_x, p_y and d_{xz}, d_{yz} transform identically as the $\Gamma_5(E)$ symmetry species leading to mixing of even and odd functions under the noncentrosymmetric ligand perturbation. In D_{3h} symmetry, it is the ($d_{x^2-y^2}$, d_{xy}) pair that transforms like (p_x, p_y) $\Gamma_6(E'')$ and defines the even-odd mixing pattern in the TBP limiting geometry. The patterns in MCD spectra arise from the combined ligand field, spin orbit, and Zeeman perturbations forming electronic states of spinor symmetry. In the limits of square (C_{4v}) and trigonal (D_{3h}) axial perturbations, the states have the spinor representations (Γ_i) shown in Scheme 7, computed as the direct product of orbital and spin representations (Koster et al., 1963). Symmetry-required mixing of states results in a transfer of the pattern of d → p intensity into the d → d ligand field spectra as shown. In lower (rhombic) symmetry, the orbital functions are mixed, and intensity is distributed over all four d → d transitions. The (−/+/−/+) alternating pattern of MCD intensity with the outer two transitions dominating in the rhombic trigonal midpoint of the pseudorotation distortion arises from a relatively large ($d_{x^2-y^2}$, d_{xy}) splitting and the large orbital moment ($L_z = 2$) of this pair of functions. Mixing of p_z is also possible for nondegenerate orbital states but contributes intensity to a lesser degree, since the spin orbit mixing required for MCD intensity will be reduced by orbital splitting.

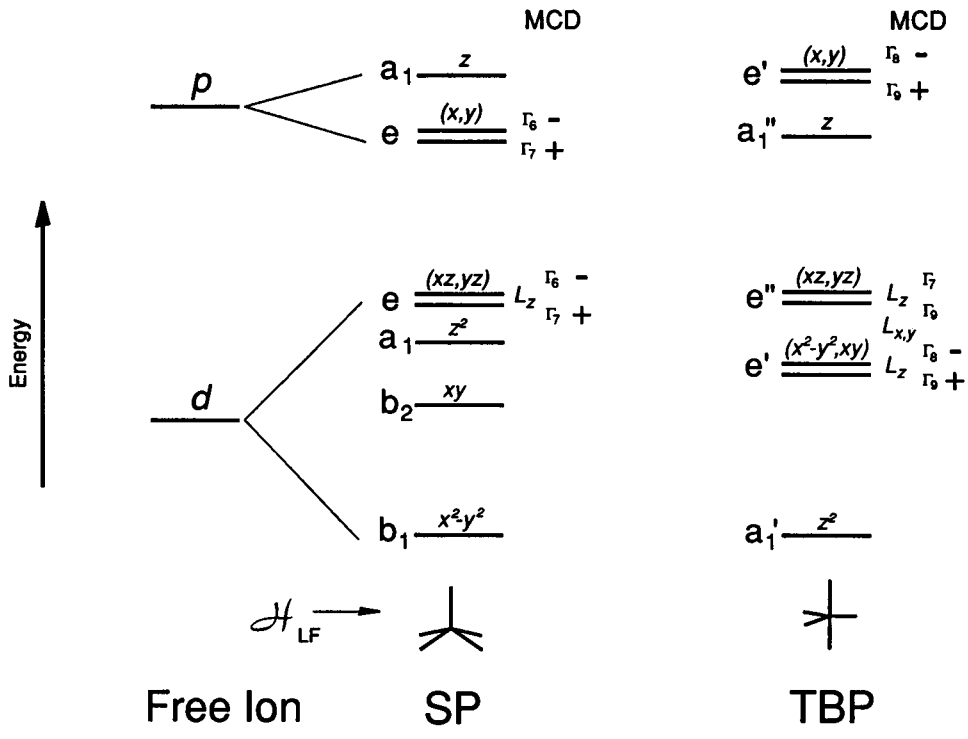

Scheme 7

Spin orbit coupling and LMCT MCD intensity

MCD intensity in d → d spectra is known to be a consequence of spin orbit mixing of ligand field wavefunctions unquenching orbital momentum in orbitally nondegenerate states. For a nondegenerate orbital ground state only weakly mixed with excited orbital states, the spin orbit mixing among excited state ligand field wavefunctions is the dominant intensity mechanism (Piepho and Schatz, 1983; Gerstman and Brill, 1985). The situation is somewhat more complicated for MCD in LMCT transitions, modeled in our ligand field calculation as d → p transitions (Fig. 2). For the isolated nondegenerate d_{z^2} ground state in the trigonal bipyramidal geometry considered in this example, orbital momentum is quenched except for spin orbit mixing of d_{xz}, d_{yz} that is revealed by the $g_\perp$ orbital g shift (Fig. 3). Calculation of the MCD in the d → p spectra for the trigonal complex (Fig. 2) leads to a prediction of a symmetrical temperature-independent A term LMCT transition MCD signal when only the final state spin-orbit contributions are considered (Fig. 2, *spectrum A*). The d_{z^2} orbital spans the a_{1g} representation of the octahedral (O_h) point group, and the A term predicted by the ligand field calculation can be directly compared with the corresponding group theoretical prediction (Stephens, 1976) for the $^2A_{1g} \rightarrow {}^2T_{1u}$ transition in an octahedral complex. This comparison emphasizes the importance of the composition of the orbital wavefunctions in determining the characteristic pattern of MCD spectra. When initial state spin orbit coupling is also active, the intensity is skewed (Fig. 2, *spectrum B*) as a result of superposition of an MCD signal arising from initial state spin orbit effects alone (Fig. 2, *spectrum C*). The latter feature represents the expression in MCD spectra of the orbital mixing that gives rise to the $g_\perp$ orbital g shift in the EPR spectrum. No MCD intensity is induced in the absence of spin orbit coupling as illustrated (Fig. 2, *spectrum D*). The transfer of intensity into the ligand field spectra is

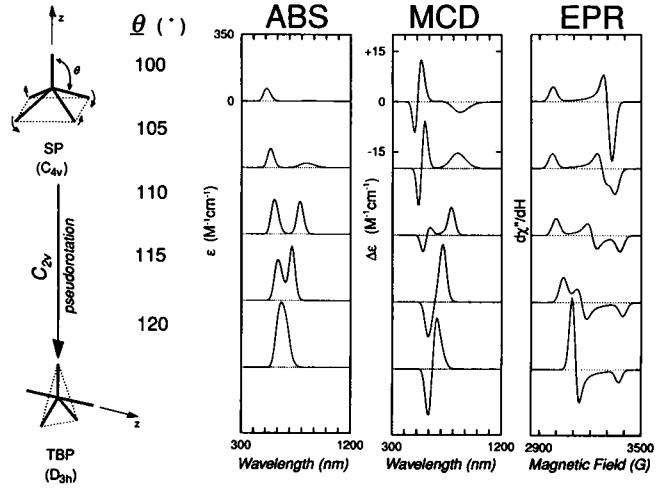

FIGURE 2 Absorption, MCD and EPR spectra computed for molecular geometries along the pseudorotation coordinate for pentacoordinate cupric complex. MCD intensities are scaled (top to bottom) ×4, ×1, ×0.2, ×0.15, and ×0.1 for ease of representation. Simulation parameters (α_2^d, α_4^d, α_1^{d-p}, α_3^{d-p}): **SP**(ax) (−28500,−12000,400,170); **SP**(eq) (−25000,-9000,400,170); **TBP**(ax) (−23000,−7500,80,62); **TBP**(eq) (−15000,−5000,100,82).

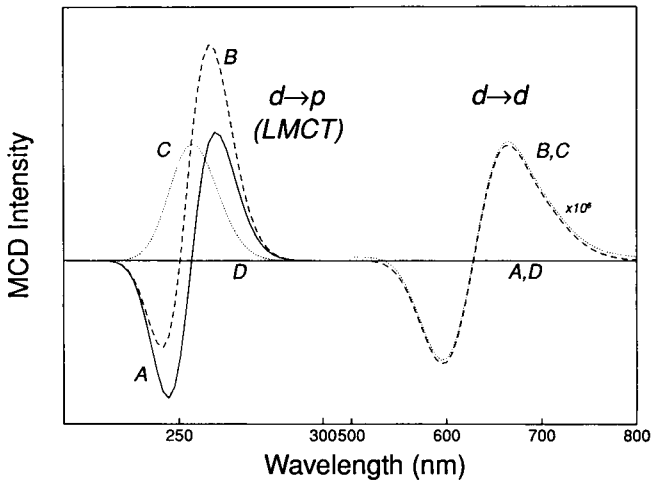

FIGURE 3 Computed MCD spectra for a trigonal cupric complex. Effect of spin orbit coupling. (*A*) $\lambda_d = 0\ cm^{-1}$, $\lambda_p = -500\ cm^{-1}$; (*B*) $\lambda_d = -500\ cm^{-1}$, $\lambda_p = -500\ cm^{-1}$; (*C*) $\lambda_d = -500\ cm^{-1}$, $\lambda_p = 0\ cm^{-1}$; (*D*) $\lambda_d = 0\ cm^{-1}$, $\lambda_p = 0\ cm^{-1}$.

independent of LMCT (d → p) excited state spin orbit interactions, and requires only spin orbit mixing over d-orbital functions. The sign of the LMCT MCD may provide the basis for assignment of the electronic transition and characterization of the CT final state, as described above for cubic symmetry.

Oriented spectra

Spectra for oriented samples, such as single crystals or membranes, are unaveraged and have a distinct appearance. In contrast to the orientationally averaged spectrum, which is a superposition of spectra arising from individuals representing all possible orientations, the oriented spectra arise from unique orientations and so can be used to determine orientations of ordered samples. A potential application to determination of orientations of chromophores in oriented lipid bilayers or on surfaces by comparison between oriented and averaged spectra is clearly a possibility.

Each of the spectra in Fig. 4 are calculated for the second structure in the pseudorotation coordinate (Fig. 3) in a unique molecular orientation with respect to the applied magnetic field. The molecular z axis is represented by the axis of the globe (Fig. 4, *upper right*) and the direction of the magnetic field is indicated by the indexing of the globe. The rhombic symmetry of the structure, an intermediate geometry in the pseudorotation, results in distinct spectra for each distinct orientation relative to the field. However, parallel and antiparallel field directions yield identical spectra (e.g., **1** and **7**), since the relation between H and **k** (and therefore E_x and E_y of the radiation field inducing the optical transition) is retained, and only the relative orientations of the molecular axes are changed. Reversing H relative to **k** by reversing the polarity of the applied magnetic field reverses the sign of the MCD signal (not shown).

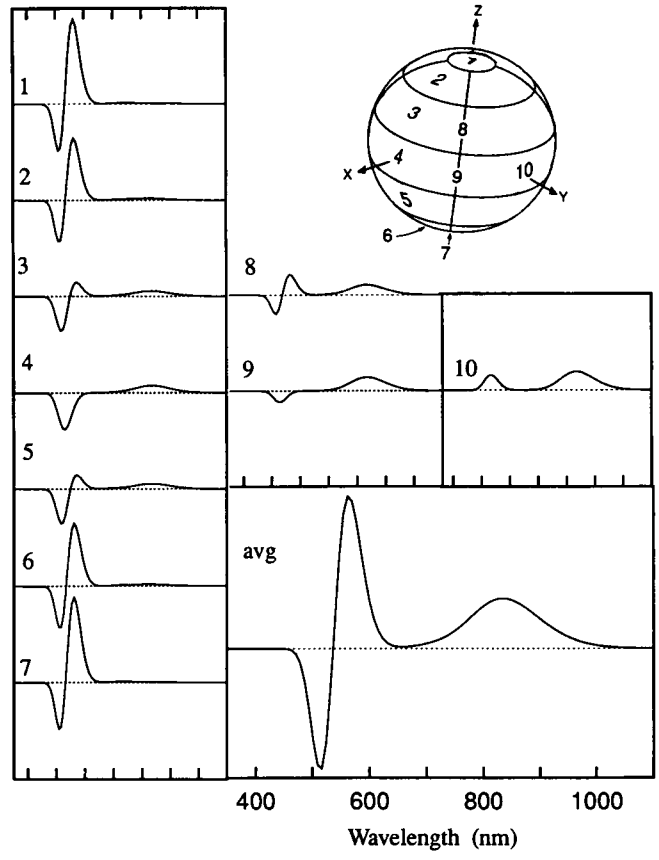

FIGURE 4 Oriented MCD spectra computed for a rhombic cupric complex. Globe (*upper right*) indicates the magnetic field orientations for each of the individual spectra (1–10). The orientationally averaged spectrum (avg) computed with an angular resolution of $\pi/8$ is shown at lower right.

Identical spectra also occur for molecular orientations related by symmetry. For example, the molecular twofold symmetry in this example results in the equivalence of spectra **2** and **6**, as well as **3** and **5**. Distinct spectra are observed for molecular orientations differing only in the value of the angle ϕ because the structure is rhombic and X and Y directions are distinct. For higher symmetry complexes (axial limiting geometries), identical spectra will result for any orientation with the same z projection of the magnetic field, reflected in azimuthal symmetry of the oriented spectra. A dramatic angular dependence of MCD intensities is illustrated in the figure, with spectra varying in magnitude along a longitude and exhibiting sign reversal over a quadrant.

Each of the spectra in Fig. 4 arising from a unique (or crystalline) orientation represents a single isolated contribution to a powder or solution spectrum, which is formed as a sum of oriented spectra from the complete statistical distribution of molecular orientations. The averaged absorption spectrum can be calculated in the absence of any preferred orientation by simply summing over linear polarizations, a consequence of the projection cosine rule for vector components. However, for MCD the average (Fig. 4, *avg*) involves cancellations of signed intensity over orientations,

and the resulting solution spectrum is the residual intensity that survives the averaging process.

Saturation of MCD

The polarizations induced in spectra arising from the Kramers doublet sublevels cancel at high temperatures, leaving the A term MCD signal that corresponds to the differential Zeeman-shifted spectra. At low temperatures and high magnetic field, when only the lowest sublevel of the electronic ground state is populated, the MCD intensity reaches its maximum value, reflecting magnetic saturation of the paramagnetic ground state. The progressive saturation of MCD signals has been shown to contain information on ground state g values that complements the information in EPR spectra and obtained from magnetochemistry (Schatz et al., 1978; Johnson and Thomson, 1980). The ligand field model for MCD permits simulation of saturation magnetization spectra for cupric complexes as illustrated by the comparison of experimental and calculated spectra in Fig. 5. The inverse geometric progression in the temperature leads to a progressive doubling of intensity to low temperature, as shown in the experimental data and reproduced in the simulation. Plotting the MCD intensity at a particular wavelength (530 nm) versus the saturation parameter ($\beta H/2kT$) generates the hyperbolic curve shown to the right of the figure on which is superimposed the experimental MCD saturation data for a synthetic complex, [Cu(PMDT)-(cresol)] (ClO_4); (PMDT = pentamethyl diethylenetriamine) (Whittaker et al., 1993).

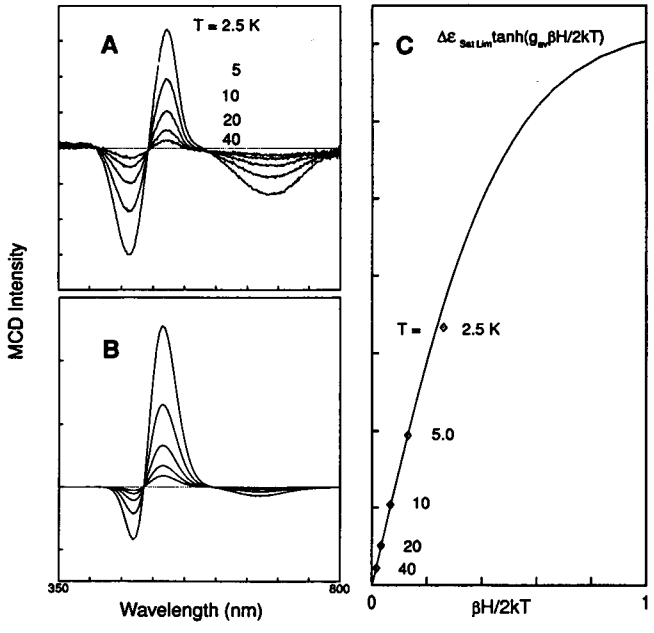

FIGURE 5 Experimental and calculated MCD saturation behavior. (*A*) Experimental data for cupric cresolate complex (H = 1 T). (*B*) Calculated MCD saturation computed at the temperatures indicated in *A*. (*C*) Saturation magnetization curve computed for the data in A with data indicated (◆).

Experimental spectra for cupric model complexes

Figs. 6 and 7 show experimental data for cupric model complexes representing tetragonal and rhombically dis-

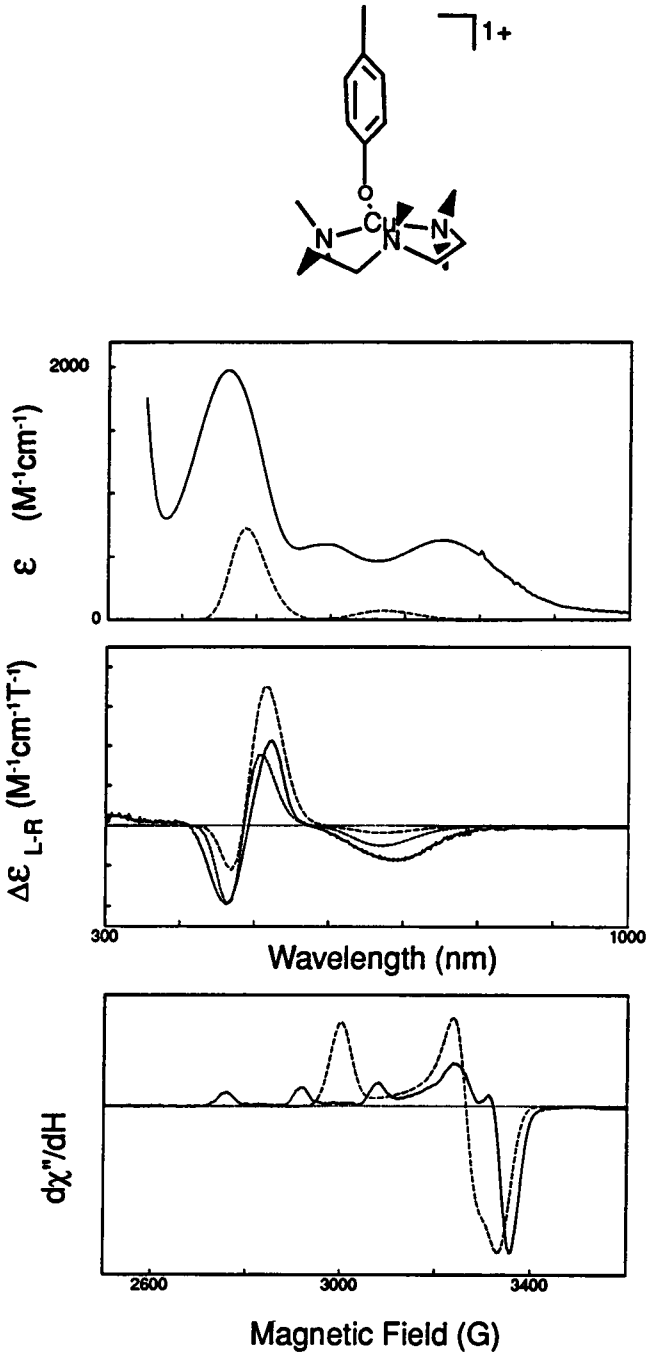

FIGURE 6 Comparison of experimental (——) and calculated (σ only: —, σ,π: ·····) low temperature absorption (*top*), MCD (*middle*) and EPR (*bottom*) spectra for the synthetic complex [Cu(PMDT)(cresol)] (ClO_4). Absorption and EPR spectra in butyronitrile:propionitrile glassing solvent at 100 K; MCD recorded for mulled sample at 4.2 K. Simulation parameters (α_2^d, α_4^d, α_1^{d-p}, α_3^{d-p}, α_1^{d-f}, α_3^{d-f}, α_5^{d-f}): O(−17700, −9600,90,20,40,16,0); N1,N3 (−15500, −8500,80,30,40,16,0); N2 (−17700, −9600,90,30,40,16,0); axial pseudoatom (−11800, −5800,90,35,40,16,0); λ_d = −475 cm^{-1}.

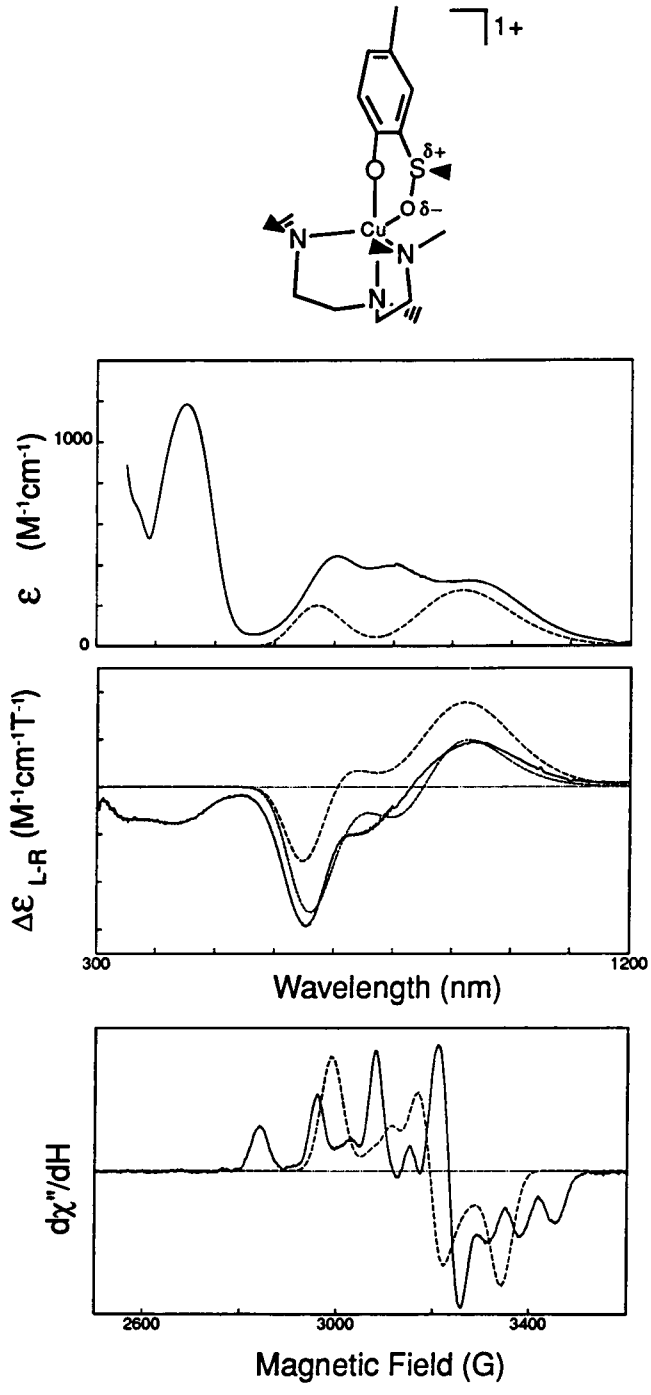

FIGURE 7 Comparison of experimental (——) and calculated (σ only: —, σ,π: ····) low temperature absorption (*top*), MCD (*middle*), and EPR (*bottom*) spectra for the synthetic complex [Cu(PMDT) (methyl sulfinylcresol)](ClO_4). Absorption and EPR spectra in butyronitrile:propionitrile glassing solvent at 100 K; MCD recorded for mulled sample at 4.2 K. Simulation parameters (α_2^d, α_4^d, α_1^{d-p}, α_3^{d-p}, α_1^{d-f}, α_3^{d-f}, α_5^{d-f}): O (ax) (−19000, −7500, 100, 45, 10, 4, 0); N (ax) (−21000, −8000, 140, 60, 10, 4, 0); N (eq) (−17000, −6500, 110, 42, 10, 4, 0); N′ (eq) (−18000, −7000, 90, 45, 10, 4, 0); O(eq) (−15000, −6000, 90, 45, 10, 4, 0); λ_d = −400 cm^{-1}.

torted trigonal geometries. The structures of the complexes have been determined crystallographically (Whittaker et al., 1993). As predicted by the model above, the square complex exhibits a pseudo-A term spectrum and the trigonal complex a more complex pattern of intensity that is consistent with cancellation of polarization for the middle pair of transitions and enhancement in the first and fourth transitions. The simulations provide a guide to insight into the information on electronic wavefunctions that is contained in spectra.

The calculations reproduce the essential features of the experimental spectra, in terms of the transition energies of the absorption spectra, the pattern of signs and intensities in the MCD spectra, and the g-shifts in the EPR spectra. The simultaneous simulation of all three spectra is performed with a single set of ligand field parameters and the crystallographically determined ligand coordinates. Deviations between the observed and calculated spectra for the inorganic complexes are not surprising, since the experimental absorption and EPR spectra are for solution samples at elevated temperature, while the computed spectra match the transition energies required by the low temperature MCD data, obtained for a mulled sample of known crystal structure.

The square $[Cu(PMDT)(cresol)]^+$ complex, a model for tyrosine phenolate interactions with cupric sites in proteins shows the largest difference between transition energies in MCD and ABS spectra (Fig. 6). The absorption bands are shifted approximately 2000 cm^{-1} to lower energy in solution, probably reflecting the relaxation of the nearly planar geometry of the crystalline complex as a consequence of solvent interactions. The experimental absorption spectrum (Fig. 6, *top*) is dominated by an intense phenolate-to-copper LMCT transition at 450 nm, with metal d → d spectra occurring to lower energy. The ligand field transitions acquire circular polarization in a magnetic field, the lower energy band becoming predominantly right-hand circularly polarized (negatively signed MCD) and the higher energy band splitting into a pair of features nearly equal intensity but oppositely signed, a pseudo-A Term (Fig. 6, *middle*). This spectrum strongly resembles the spectrum computed for the square pyramidal limit of the pseudorotation coordinate (Fig. 2), emphasizing that MCD spectra reveal the effect of geometric factors on electronic wavefunctions in a complex. No MCD intensity is associated with the strong LMCT transition, which is understandable in terms of the orbitally nondegenerate character of the LMCT final state, approximately described as a phenoxyl radical associated with a full shell (d^{10}) cuprous ion, accounting for the weak intensity in the LMCT band. Simulation of MCD spectra for this complex using the crystallographic ligand positions was less satisfactory than the others described below, in that an additional axial perturbation, not accountable for in terms of ligand positions, was required to achieve the level of agreement shown. This difficulty may reflect a limitation of the ligand field description, lattice interactions not taken into account in the ligand position data, or it might indicate that σ LMCT is not the dominating intensity mechanism in this complex. The EPR spectrum of the complex (Fig. 6, *bottom*) reflects the axial structure in the $g_{\|} > g_{\perp} > 2$ characteristic

of a $d_{x^2-y^2}$ orbital contribution. The calculated EPR spectrum closely reproduces the orbital g-shifts in the experimental spectrum, and the most distinctive difference between the experimental and simulated spectra are the absence of electron-nuclear hyperfine splittings from the copper nucleus in the simulation, since this interaction is not included in the calculation.

The discrepancy between experimental and simulated MCD spectrum calculated within the σ LMCT p-mixing model reveals a deficiency of the ligand field wavefunctions when π LMCT is neglected. Since π LMCT is expected to contribute to MCD of opposite sign of σ LMCT ($^2T_{2g} \rightarrow {}^2T_{1u}$ (σ) and $^2T_{2g} \rightarrow {}^2T_{2u}$ (π) give rise to oppositely signed C Terms (Stephens, 1966; Piepho and Schatz, 1984)), neglecting this contribution in the model leads to a skewing of the simulated MCD spectra to positive intensities. The offset of the MCD spectrum (Gerstman and Brill, 1985), defined as the excess circular polarization for the sum over signed MCD intensities of the d $\rightarrow$ d bands, results from rhombic mixing of d_{xz}, d_{yz}, and d_{xy} orbital contributions into $d_{x^2-y^2}$ and d_{z^2} orbital ground states of the cupric ion. The former components give rise to excess positive or negative MCD intensity depending on whether the intensity derives predominantly from σ or π LMCT (compare discussion of Fig. 1). Including π LMCT contributions through expansion of the basis set with f-orbitals (which span the T_{2u} representation in O_h symmetry) allows the intensities to be accurately fit to experiment (Fig. 6, *middle*).

The solution MCD spectrum for the [Cu(PMDT)(methylsulfinylcresol)]$^+$ (not shown) matches the MCD of the mulled crystal sample (Fig. 7, *middle*), suggesting that this complex undergoes less extensive structural change in solution, as might be expected for a coordinately saturated metal complex. The complex is typical of a trigonally coordinated copper with axial interactions dominating, reflected in the relatively short Cu-N(amine) and Cu-O(phenolate) bond distances (Whittaker et al., 1993). Electronic transitions lie at relatively low energy, a consequence of the relatively weak overall metal-ligand interactions characteristic of the trigonal ligand arrangement. Calculations based on a strong axial perturbation resulting from an axial compression of a trigonally distorted complex reproduce the transition energies in absorption. The pattern of MCD intensity for this complex resembles that calculated for the rhombic midpoint in the pseudorotation coordinate (Fig. 2), once again reinforcing the strong connection between geometric and electronic factors in determining MCD spectra. The optical spectra is roughly reproduced in terms of the energy splittings, although the match in intensity is poor for wavefunctions that correctly give the observed pattern of MCD intensity. These examples illustrate how the patterns of MCD intensity reveal patterns in electronic wavefunctions. The distinctive ground state EPR spectrum recorded for this complex reflects the strong trigonal perturbation of the cupric ion, consistent with the eigenvector analysis in the calculation, which indicates a predominantly (0.92) d_{z^2} orbital contribution in the ground state wavefunction. The spectrum has previously been simulated by a spin Hamiltonian analysis providing estimates of the g values (g_{xx} = 2.22, g_{yy} = 2.10, g_{zz} = 2.01) that are closely reproduced in the ligand field model calculation (2.25, 2.11, 2.01) using the same spin orbit coupling constant that was effective in simulating the EPR g-shifts of the square complex. However, the ligand field wavefunctions that reproduce the experimental MCD spectrum (Fig. 6, *middle*) somewhat overestimate the largest orbital g-shift in the EPR simulation. This most likely reflects the deficiencies of the ligand field wavefunctions, but it is again worth noting that the MCD is recorded for a mulled crystalline sample, while the EPR data are obtained for a solution sample.

Spectra for the azide adduct of the copper metalloenzyme galactose oxidase are shown in Fig. 8. The structure of the enzyme-active site is known at nearly atomic resolution from x-ray crystallographic studies (Ito et al., 1991) which show the copper coordinated by four protein sidechains and a single solvent (X = water or hydroxide) or exogenous ligand. Crystallographic studies indicate that the ligand environment is not dramatically changed on forming anion complexes with, e.g., acetate replacing water in the active site (X = acetate). Previous spectroscopic studies have shown that the active site of galactose oxidase is quite flexible and undergoes a reversible, temperature-dependent conformational change that can be described as a pseudorotation (Whittaker and Whittaker, 1993); (Whittaker, 1994). The pseudorotation coordinate of the enzyme-active site involves strengthening metal-exogenous ligand interactions with displacement of the unmodified tyrosinate (Tyr495). This conformational change, organized around a T-shaped framework of essentially rigid ligands (His496, His581, and Tyr272) appears to be important for defining a proton transfer coordinate that may serve to activate substrate in the catalytic mechanism (Whittaker and Whittaker, 1993). Low temperature spectra of the enzyme reflect this change in the copper environment, and anion binding appears to completely convert the enzyme to this limiting form, reflecting the displacement of the unmodified Tyr495 from the axial position in the complex as determined spectroscopically (Whittaker, 1993). The MCD spectrum of the azide complex (Fig. 7, X = N_3^-) strongly supports a strong axial perturbation of the active site copper complex associated with the appearance of a pseudo-A term in the ligand field region ($\Delta\varepsilon_{560}$ = -15 $M^{-1}cm^{-1}T^{-1}$, $\Delta\varepsilon_{620}$ = $+10$ $M^{-1}cm^{-1}T^{-1}$, $\Delta\varepsilon_{730}$ = -9 $M^{-1}cm^{-1}T^{-1}$). The spectrum of this limiting form of the enzyme can be directly compared with the results of calculations on idealized square-pyramidal models and the tetragonal-axial synthetic complex. The ground state eigenvector computed in the ligand field calculation reflects the lower symmetry of the enzyme complex in the mixed orbital coefficients (0.88 $d_{x^2-y^2}$, 0.1 d_{yz}) consistent with significant rhombicity in the coordination environment. The transition that gives rise to the intense negatively signed MCD at higher energy has previously been assigned as π LMCT for the equatorially coordinated azide, the near-degeneracy (π_x, π_y) of the

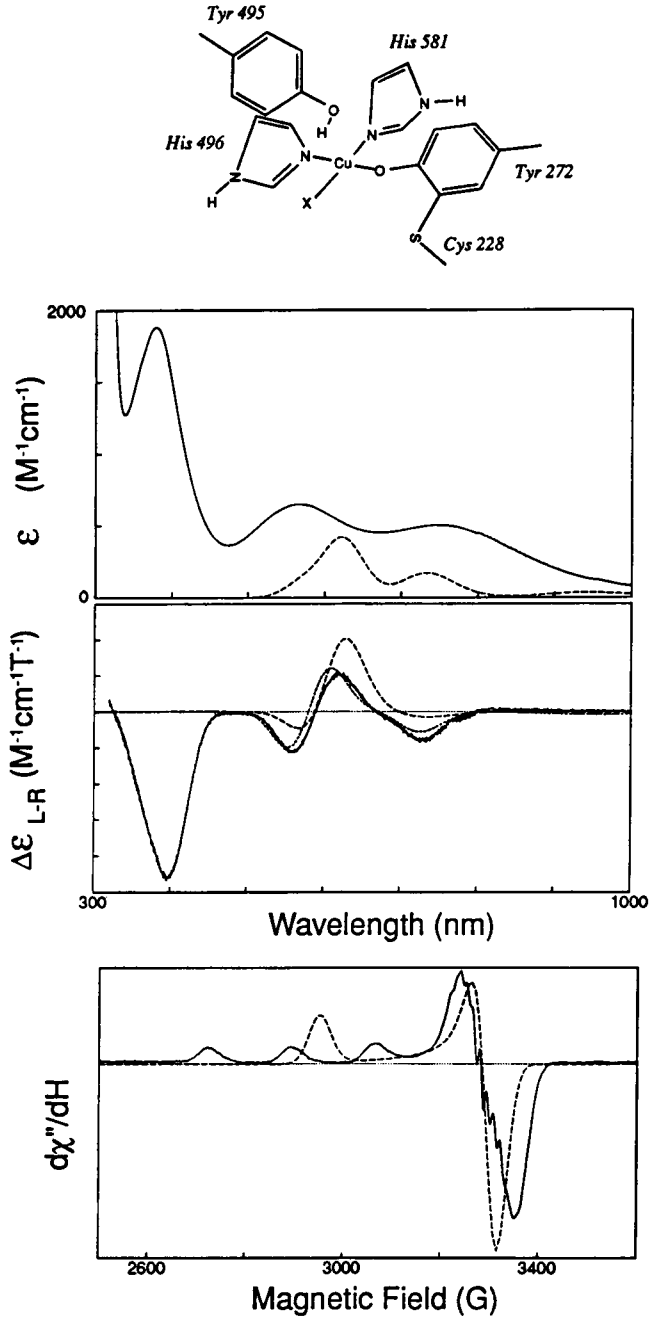

FIGURE 8 Comparison of experimental (——) and calculated (σ only: —, σ,π: ····) room temperature absorption (*top*), and low temperature MCD (*middle*) and EPR (*bottom*) spectra for the azide complex of galactose oxidase. Absorption spectrum recorded in aqueous solution (50 mM $NaHPO_4$ buffer pH 7); MCD recorded for sample in 50% glycerol/H_2O glassing solvent at 4.2 K; EPR recorded for enzyme in frozen aqueous solution at 120 K. Each sample prepared in presence of saturating concentrations of Na azide. Simulation parameters (α_2^d, α_4^d, α_1^{d-p}, α_3^{d-p}, α_1^{d-f}, α_3^{d-f}, α_5^{d-f}): O (272) (−10800, 6500, 80, 33, 40, 40, 1); O (495) (−4000, −2300, 80, 30, 40, 40, 1); N (496) (−10800, −6500, 110, 50, 40, 40, 1); N (581) (−10800, −6500, 80, 33, 40, 40, 1); N (azide) (−12400, −7600, 120, 55, 40, 40, 1); $\lambda_d = -400\ cm^{-1}$.

LMCT final state providing a mechanism for MCD. The sign of the MCD intensity is consistent with this assignment of π character in the allowed transition on the basis of the earlier discussion regarding the information in the sign of the MCD C term. A clearer picture emerges from the combined spectroscopic studies supported by the ligand field intensity calculation of a tetragonal axial ligand perturbation of the copper in the azide adduct, confirming earlier structural interpretations of this enzyme complex (Whittaker and Whittaker, 1993).

Outlook

The ligand field model appears to be an effective tool for developing insight into MCD spectra for biological cupric complexes, contributing to a clearer understanding of the electronic structural features of the metal center. This modeling approach gives insight into the nature of electronic wavefunctions for a cupric ion bound to a protein, an essential first step to understanding the structural origins of catalytic chemistry. Simultaneous fitting of absorption, MCD, and EPR spectra places much more severe constraints on the model than any single simulation or reproducing energy splittings alone, since each approach is sensitive to a different aspect of electronic structure.

Further extensions of the model to high spin complexes of Mn^{3+} (d^4) and Fe^{2+} (d^6) ions (respectively, one hole or one electron outside of a half-filled shell) can be expected to be fruitful. The present studies already provide insight into the unusual pattern of MCD intensity observed in the Mn^{3+} active site complex of Mn superoxide dismutase (Whittaker and Whittaker, 1991), for which a trigonal bipyramidal geometry is indicated by x-ray crystallographic studies (Stallings et al., 1984; Ludwig et al., 1991). The MCD spectrum is a pattern of alternating signs with the transitions at highest and lowest energies dominating the spectra. This corresponds to the pattern computed for the rhombic-trigonal intermediate geometry in the pseudorotation diagram (Fig. 2) and experimentally recorded for the [Cu(PMDT) (methyl sulfinylcresol)] model compound, but with reversed signs as expected for Mn^{3+} for which the spin orbit coupling constant $\lambda_{Mn^{3+}}$, free ion $\sim +90\ cm^{-1}$, opposite in sign to that for copper. MCD spectra previously reported for a square pyramidal $[MnCl_5]^{2-}$ complex again show the same pattern of intensity as predicted and observed for square pyramidal Cu^{2+} but again reversed in sign as a consequence of the oppositely signed spin orbit terms. The latter example is of special interest in that the allowing LMCT are also observed in the experimental spectrum. The same pseudo-A term signature appears in both the allowed LMCT and the forbidden d → d spectra, supporting the analysis outlined above for the transfer of patterns of MCD intensity from allowed into forbidden spectra through mixing ligand field and charge transfer wavefunctions. Further insights are expected as the range of applications expands. By revealing essential features of electronic wavefunctions, MCD extends the spectroscopic information available from absorption and EPR measurements. The combination of all three approaches (ABS, MCD, and EPR) is required for insight

into the nature of biological copper complexes at the electronic structural level of resolution that will establish a fundamental connection with chemistry.

The authors would like to thank Dr. M. M. Whittaker for preparation of synthetic and protein samples used in experiments described in this paper. Support from National Institute of Health grant GM-46749 (to J. W. W.) is gratefully acknowledged.

REFERENCES

Ballhausen, C. J. 1962. Introduction to Ligand Field Theory. McGraw-Hill, San Francisco.

Ballhausen, C. J. 1979. Molecular Electronic Structures of Transition Metal Complexes. Wiley, New York.

Ballhausen, C. J. and H. B. Gray. 1964. Molecular Orbital Theory. Benjamin/Cummings, Reading.

Berry, R. S. 1960. Time-dependent measurements and molecular structure: ozone. *Rev. Mod. Phys.* 32:447–454.

Companion, A. L., and M. A. Komarynsky. 1964. Crystal field splitting diagrams. *J. Chem. Educ.* 41:257–262.

Eyring, H., J. Walter, and G. E. Kimball. 1944. Quantum Chemistry. John Wiley, New York.

Gaunt, J. A. 1929. The triplets of helium. *Phil. Trans.* 228A:151–196.

Gerstman, B. S. and A. S. Brill. 1985. Magnetic circular dichroism of low symmetry cupric sites. *J. Chem. Phys.* 82:1212–1230.

Griffith, J. S. 1964. The Theory of Transition-Metal Ions. Cambridge University Press, Cambridge.

Ito, N., S. E. V. Phillips, C. Stevens, Z. B. Ogel, M. J. McPherson, J. N. Keen, K. D. S. Yadev, and P. F. Knowles. 1991. 1.7 Å Crystal structure of galactose oxidase from *Dactylium dendroides*. *Nature (Lond.)* 350: 87–90.

Johnson, M. K., A. E. Robinson, and A. J. Thomson. 1982. Low-temperature magnetic circular dichroism studies on iron-sulfur proteins. *In* Iron Sulfur Proteins. T. Spiro, editor. Wiley Interscience, New York. 367–406.

Johnson, M. K. and A. J. Thomson. 1980. Magnetization curves of hemoproteins measured by low-temperature magnetic circular dichroism spectroscopy. *Biochem. J.* 191:411–420.

Kaden, T. A. 1974. Magnetic circular dichroism studies of the active site geometry in metalloenzymes. *In* Metal Ions in Biological Systems, Vol. 1. H. Sigel, editor. Marcel Dekker, New York. 1–27.

Koster, G. F., J. O. Dimmock, R. G. Wheeler, and H. Statz. 1963. Properties of the Thirty-Two Point Groups. M.I.T. Press, Cambridge.

Lever, A. B. P. 1984. Inorganic Electronic Spectroscopy, 2nd ed. Elsevier, New York.

Ludwig, M. L., A. L. Metzger, K. A. Pattridge and W. C. Stallings. 1991. Manganese Superoxide from *Thermus thermophilus*. A structural model refined at 1.8 Å resolution. *J. Mol. Biol.* 219:335–358.

Moore, C. E. 1952. Atomic Energy Levels. National Bureau of Standards Circular 467, Vol. II. National Bureau of Standards, Washington, D.C.

Muertterties, E. L., and L. J. Guggenberger. 1974. Idealized polytopal forms. Description of real molecules referenced to ideal polygons or polyhedra in geometric reaction path form. *J. Am. Chem. Soc.* 96: 1748–1756.

Piepho, S. B. and P. N. Schatz. 1983. Group theory in spectroscopy with applications to magnetic circular dichroism. Wiley Interscience, New York.

Press, W. H., S. A. Teukolsky, W. T. Vettering, and B. P. Flannery. 1992. Numerical recipes in C. Cambridge University Press, Cambridge.

Schatz, P. N., R. L. Mowery, and E. R. Krausz, 1978. MCD/MCPL saturation theory with application to molecules in $D_{\infty h}$ and its subgroups. *Mol. Phys.* 35:1537–1557.

Stallings, W. C., K. A. Pattridge, R. K. Strong, and M. L. Ludwig. 1984. Manganese and iron superoxide dismutases are structural homologs. *J. Biol. Chem.* 259:10695–10699.

Stephens, P. J. 1965. The Faraday rotation of allowed transitions: charge transfer transitions in $K_3Fe(CN)_6$. *Inorg. Chem.* 4:1690–1692.

Stephens, P. J. 1976. Magnetic circular dichroism. *Adv. Chem. Phys.* 35:197–265.

Sutherland, J. C., and B. Holmquist. 1980. Magnetic circular dichroism of biological molecules. *Ann. Rev. Biophys. Bioeng.* 9:293–326.

Van Vleck, J. H. 1932. Theory of the variations in paramagnetic anisotropy among different salts of the iron group. *Phys. Rev.* 41:208–215.

Vickery, L. E. 1978. Spin states of heme proteins by magnetic circular dichroism. *Methods Enzymol.* 54:284–302.

Weissbluth, M. 1978. Atoms and Molecules. Academic Press, New York. 326.

Whittaker, J. W. 1994. The free radical coupled copper active site in galactose oxidase. *In* Metal Ions in Biological Systems, Vol. 30. H. Sigel, editor.

Whittaker, J. W. and M. M. Whittaker. 1991. Active site spectral studies on manganese superoxide dismutase. *J. Am. Chem. Soc.* 113:5528–5540.

Whittaker, M. M., Y. Y. Chuang, and J. W. Whittaker. 1993. Models for the redox active site in galactose oxidase. *J. Am. Chem. Soc.* 115: 10029–10035.

Whittaker, M. M. and J. W. Whittaker. 1988. The active site of galactose oxidase. *J. Biol. Chem.* 263:6074–6080.

Whittaker, M. M. and J. W. Whittaker, 1993. Ligand interactions with galactose oxidase: mechanistic insights. *Biophys. J.* 64:762–772.

Zare, R. N. 1988. Angular Momentum. Wiley Interscience, New York.